Preprint to be published in Earth and Planetary Science Letters.

MICROCRATERS FORMED IN GLASS BY LOW DENSITY PROJECTILES

by

J.-C. Mandeville*

and

James F. Vedder

Planetology Branch

Space Science Division

NASA-Ames Research Center

Moffett Field, California 94035

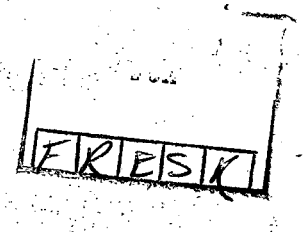

*On leave from the Office National D'Etudes et de Recherches Aerospatiales under a [illegible] from the European Space Research Organization.

MICROCRATERS FORMED IN GLASS BY LOW DENSITY PROJECTILES

ABSTRACT

Microcraters were produced in soda-lime glass by the impact of low density projectiles of polystyrene ($\rho = 1.06$ g/cm^3) with masses between 0.7 and 62 picograms and velocities between 2 and 14 km/s. The morphology of the craters depends on the velocity and angle of incidence of the projectiles. For normal incidence at 3 km/s, the projectile leaves a dent; and at 4 km/s the deformed projectile lines the depression and forms a rim. For velocities greater than 5.2 km/s at normal incidence, an extensive spallation zone surrounds the central pit; the ratio of the central pit diameter to the projectile diameter (D_c/d) increases from 1.25 to 1.75 with increasing velocity; and D_c/d is independent of projectile mass for constant velocity. The transitions in morphology of the craters formed by polystyrene spheres occur at higher velocities than they do for more dense projectiles. For oblique impact, the craters are elongated and shallow with the spallation threshold occurring at higher velocity. For normal incidence, the total displaced mass of the target material per unit of projectile kinetic energy increases slowly with the energy, according to the relation:

$$M_e/E = 227\ E^{0.135} \text{ picogram/microjoule}$$

INTRODUCTION

Experimental studies of microcraters formed by hypervelocity impacts have become increasingly important in recent years. Fundamental developments and verification of theories for cratering depend on impact

experiments in the laboratory. Current impetus results from the fact that the flux of interplanetary particles may be derived from the number and size of craters on detectors flown on spacecraft (1) or on recovered parts of spacecraft (2). For these determinations, a relationship between projectile size and crater size is required as well as knowledge of morphological features that distinguish a true event from other damage (3). Estimates of useful lifetimes of sensitive parts of spacecraft exposed to erosion by micrometeoroids are based on simulation experiments (4). Also, meteoroids and planetary bodies without an atmosphere undergo bombardment by interplanetary dust (5, 6, 7) and estimates of the cumulative effect on these bodies depends on experimental evidence. Of particular recent interest is the application of laboratory data in the derivation of fluxes and erosion rates from the microcraters found in abundance on lunar samples (8, 9) returned by the Apollo 11 and Apollo 12 missions.

Most of the previous experimentation in the formation of craters by hypervelocity microspheres has been done with metal projectiles impacting metal targets (10, 11, 12). Very little work has been done with nonmetallic targets (9, 13, 14), and no work is known for nonmetallic projectiles in the micrometer-size range. Metal projectiles, however, are not typical of the secondary particles in the lunar environment (5) or of the interplanetary dust which may have primarily a low-density, stony composition (7). For this reason, an experimental program is in progress at Ames Research Center to study microcraters generated in simulated lunar materials by projectiles of various densities and compositions. This report contains results on craters in soda-lime-silica

glass formed by polystyrene spheres (ρ = 1.06 g/cm^3) between 1 and 5 μm in diameter with velocities from 2 to 14 km/s. Polystyrene was used in an attempt to simulate the low density component of particulate material that may exist in interplanetary space.

PROCEDURE

A vertically oriented microparticle accelerator of unique design provided the hypervelocity, low-density projectiles for the experiment. At the upper end, single particles are charged by ion bombardment in high vacuum in an electrodynamic suspension system (15). The charged particle is injected into the accelerator having four drift tubes, each initially at a high negative voltage. Each tube is grounded in sequence at the proper time to give four stages of acceleration with a total voltage equivalent to about 1.5 MV. The timing sequence is automatically controlled by the particle's charge-to-mass ratio measured in the source by the operator just prior to ejection. At the entrance to the accelerator, the particle generates a signal on a detector to initiate the timing sequence. Detectors in the target chamber record the passage of the projectile and provide information on its charge, velocity, and impact site (16). The craters usually lie within a circle of 1 mm radius. A rotary table permits the remote selection of different targets and the separation of ranges of impact parameters on a particular target. For impact angles other than normal (θ = 90°), the targets are mounted on blocks machined to the appropriate angle.

Once a series of impacts is completed, the targets are scanned optically to locate each crater and the impact areas marked for later

examination in a scanning electron microscope (SEM). The crater sites are correlated with the position data from the detector for assignment of impacting mass and velocity. In cases of doubtful correlations, the crater size and morphology are an aid in the identification. Impacts are limited to about six per target site to assure the correct identification. Photomicrographs of each crater are taken with the SEM with the stage tilt angle (T) at 23° and 30° relative to the horizontal plane to provide a stereoscopic view. Crater depths are determined photogrammetrically, and the stereopsis clarifies details in the crater morphology. A thin vapor-deposited film of gold is applied to the target prior to examination in the SEM in order to obtain a good image. In some micrographs, a slight crazing of the gold film may be noted.

RESULTS

In this study, we impacted polystyrene spheres on soda-lime-silica glass. The glass targets were made from ordinary microscope slides with a thickness of 1 mm and a density of 2.48 g/cm^3. The polystyrene has an additive of 8% divinylbenzene as an agent for crosslinking the molecular chains. The material density is 1.06 g/cm^3; and under normal conditions, the particles are infusible. Spheres with diameters between 1 μm and 5 μm and masses between 0.7 and 62 pg were accelerated to velocities between 2 and 14 km/s. In general, the small particles have the highest velocities, a consequence of the charging process (15). Most of the impacts were at an incident angle (θ) of 90° relative to the glass surface. The others were at impact angles of 45° and 30°. Primary and derived data for the projectiles and craters are tabulated for normal incidence in table 1 and for oblique incidence in table 2.

The accuracy of the measurements can be evaluated and estimates of the probable errors assigned to the various quantities. The projectile mass, derived from the projectile charge and charge-to-mass ratio, has an error of 10%. The projectile diameter, calculated from its mass and density, then has a probable error of ± 3.3%. The polystyrene particles are assumed to remain spherical in the charging and acceleration process, and the symmetry of the craters for $\theta = 90°$ substantiates the assumption. In a preliminary study, polyethylene spheres ($\rho = 0.915$ g/cm), which did not retain their sphericity in the charging process, formed unusual and highly asymmetrical craters. The velocities have a probable error of about ± 5%. From the errors for mass and velocity, we derive an error of ± 12% for the kinetic energy of the projectile. Crater dimensions measured on the photomicrographs from the SEM have a ± 5% probable error as a result of uncertainty in the magnification. We have taken the diameter of the spallation region to be an average of a maximum and minimum diameter of an area that is often very asymmetric; and, therefore, a value for the accuracy has little meaning. The crater depth derived from measurements on stereographic pairs of micrographs has a probable error of ± 50%. The error in the volume of ejected material is about ± 60%, depending primarily on the uncertainty in the depth and secondarily on the deviation of the shape of the crater from the shape used to calculate the crater volume. No correction is made for the thickness of projectile material on the crater floor.

The examination of the SEM micrographs reveals several morphological features that change with the impact velocity and angle of incidence of the projectile. Consider, first, impacts at normal incidence. Six

examples are shown in fig. 1. For a velocity of 2.95 km/s, there is only a smooth indentation in the glass surface (fig. 1a) with a diameter smaller than the projectile diameter. The projectile has rebounded from the surface leaving a very shallow crater. Surrounding it is a slightly raised, smooth rim generated by the plastic deformation of the glass. A crater for a 2.06 km/s projectile could not be located because it was either too small and shallow for detection or did not exist for that velocity. At 4.15 km/s, the projectile lines the circular cup and spreads into a narrow continuous lip (fig. 1b). The pit diameter equals the projectile diameter. There are no radial or concentric fractures outside the lip. For velocities between 4.9 and 5.1 km/s, we observe a circular, shallow cup ringed by a petalled lip of projectile material (fig. 1c). Some of the petals extend as much as 0.6 μm above the surface. Again, there are no fractures outside the lip. At velocities exceeding 5.2 km/s, an extensive spallation zone develops around the central pit (figs. 1d, 1e, and 1f). This zone is characterized by approximately radial and concentric fractures. Where the individual spalls have been ejected, radial ridges appear beneath the locations of the radial surface cracks. At a given velocity of impact, a larger projectile usually will dislodge completely a greater number of the spalls. The larger ejected spalls may remove the outer part of the cup and reduce its diameter. In such cases, an annular depression is left outside the cup (fig. 1d). The remaining spalls may rest more than 1 μm above the glass surface. At impact velocities exceeding 7 km/s, almost all of the petalled lip has been carried away by a ring of ejected spalls as in fig. 1e. The spallation zone has become more

finely fragmented, and the smaller spalls are missing from the inner ends of the larger segments. The relative depths of the craters increase with the velocity of impact. In part, this is a result of increased or complete dispersion of the projectile material in and from the pit. The cross section of the central cup is approximately hemispherical.

For impacts at a 45° angle of incidence, the crater pit and spallation zone become asymmetrical (fig. 2a). At velocities less than 6 km/s, we find the cup is broadened toward the forward end, "down range" from the point of impact. The greatest width occurs about 2/3 the length of the cup from the rear end. In profile, the crater is shallow and nearly semi-ellipsoidal in the long direction. The lip of projectile material at the forward end may be raised as much as 1.5 μm above the glass surface. There is no radial fracturing or spallation in this velocity range. At an impact velocity of 6.5 km/s spallation develops. Recall that for $\theta = 90°$ the spalls occurred for velocities exceeding 5.2 km/s. The spallation zone usually predominates at the forward end but may sometimes be nearly circular. In the velocity range of 5.8 to 6.8 km/s, the crater profile changes such that the greatest depth occurs closer to the "up range" crater rim.

The damaged area is even more asymmetrical for an angle of incidence of 30°. Up to a velocity of 12.3 km/s, we find little spallation; although for velocities between 7 and 8 km/s, a few spalls may be generated (fig. 2b). The craters are shallower relative to those formed at $\theta = 45°$. The damaged area is about the same as in the 45° impacts, but the crater is more elongated. At velocities less than 7 km/s, small

droplets with diameters of about 0.1 to 0.15 μm fan out from the impact point. These are probably projectile material. The results for oblique impacts indicate that the crater depth and the threshold for spallation are determined by the normal component of velocity and that the asymmetry of the crater is controlled by the tangential component.

Some of the targets, after the SEM examination, were treated in a low-temperature asher in an attempt to remove projectile material and thus to distinguish it from target material. The material is exposed in the asher to monatomic oxygen at controlled temperatures. By this procedure, the lips were reduced in height or removed almost entirely. Prior to this treatment, the gold film applied for the SEM image was wiped off; but in some cases, where part of the crater floor was still coated with the film, the gold appeared to lie slightly above the floor on a thin layer of the polystyrene which was protected from the ashing process by the gold film. Thus, our conclusions on the distribution of projectile material in the crater and in the petalled lip are substantiated.

Figure 3 shows a graph of the ratio of the crater diameter to the projectile diameter (d) versus velocity. The diameter of the central cup is denoted D_C and the average diameter of the spallation zone D_S. A maximum and minimum diameter are measured and averaged to give D_S. For velocities from 5.2 to 14 km/s, the ratio D_C/d increases from 1.25 to 1.75. A least squares fit to the data in this velocity range gives $D_C/d = 0.76\ v^{0.315}$ where v is the projectile velocity in kilometers per second. Because of inherent limitations of the particle charging system, the projectile mass is, in general, smaller for projectiles with the higher velocities. But the mass or, equivalently, size does not

influence the D_c/d ratio noticeably. This is more clearly shown in fig. 4, where D_c/d is plotted against the mass of the projectile for several velocity intervals. In each range, the ratio is constant within the accuracy of the data. The mean values for D_c/d are 1.27 for velocities between 5.3 and 6.4 km/s, 1.47 for 7 to 10 km/s, and 1.71 for 12-14 km/s. In the 5.3 to 6.4 km/s range of velocities, the mass varies from 2.5 to 46 picograms. Thus, in our data there is no discernable mass, or scale, effect on the diameter of the central pit other than that caused by the change in projectile diameter with the mass. At velocities below 5.2 km/s, where spallation does not occur, the diameter ratio drops off more rapidly. This is the result of a thicker lining of projectile material in the pit, the uncertainty in defining the cup diameter for measurement in these cases, and a transition in the cratering process.

In fig. 5, we have plotted the crater diameter versus the mass of the projectile for the same velocity intervals. Equations from a least squares fit to the data in these ranges indicate that for constant velocity the diameter of the central cup varies approximately as the cube root of the mass of the projectile and, therefore, as the diameter of the projectile. This result is equivalent to that seen in fig. 4 where D_c/d is constant for a given velocity. The equations for the spallation data is these velocity intervals indicate a slight increase in the ratio of diameter-to-projectile-diameter as the projectile mass increases.

The main features in the changing morphology of the craters examined here may be compared to those observed in other studies of impacts by microparticles on soda-lime glass. Information is available for impacts on glass by aluminum projectiles (14) and by iron projectiles (9).

For the latter, target indentation with rebound of the projectile occurs at velocities of impact less than 1 km/s. With the polystyrene particles, a dent occurs at 3 km/s. A deformed iron projectile rests in the crater for impact velocities between 1 and 2 km/s, and spallation has developed at 3 km/s. With polystyrene, a highly deformed projectile overflows the crater at 4 km/s and spallation appears at velocities exceeding 5.2 km/s. Impacts by aluminum projectiles generate spallation at a velocity of 3.6 km/s, but the threshold velocity was not investigated. The preceeding information is summarized in table 3. These comparisons show that the velocity thresholds for the morphological transitions are some direct function of the specific energy ($1/2\ \rho\ v^2$) of the projectiles; that is, higher velocities are required for low density projectiles to generate the same effects as those generated by impacts of high density particles.

A study by Bloch et al. (13) of craters formed by iron projectiles impacting quartz glass provides additional data for comparison. Within several velocity intervals between 2.8 and 8 km/s, their ratio, D_c/d, is nearly independent of the mass of the iron projectile. This is the same result as determined for polystyrene impacting glass. In contrast, their D_c/d ratio increases as the 0.67 power of velocity; while in our case, the exponent is only 0.315. Their value of 2.2 for D_c/d at 20 km/s compares favorably with an extrapolated value of 1.95 at 20 km/s for polystyrene impacting glass. Because of the difference in the densities of iron and polystyrene, the actual crater size is larger for a polystyrene projectile with the same mass and velocity as an iron projectile. The curves cross near 14 km/s, but diverge rapidly at higher and lower velocities.

It is interesting to relate the mass of target material displaced (M_e) to the kinetic energy (E) of the impacting projectile for comparison with other experiments. The volume of the crater can be approximated by the volume of a spherical segment of depth P and diameter D. Thus $V = \frac{1}{6} \pi P (P^2 + \frac{3}{4} D^2)$. Using a density of 2.48 g/cm^3 for the glass, we obtain the displaced mass which is plotted against the projectile energy in fig. 6. No adjustment is made in the measured depth for the thin layer of projectile material lining the crater floor. The total displaced mass includes the spallation zone and the central cup. Not all the listed impact events were measured for depth. Also, in the normal charging process, the higher velocity projectiles have the lower energies except where a range of masses is selected for a given velocity. The least squares fit to these data give $M_{eS} = 227\ E^{1.135}$ for the total damaged region and $M_{eC} = 47\ E^{1.107}$ for the pit, where M_e is in picograms and E in microjoules. Thus, the displaced mass per unit of projectile energy increases with increasing energy; that is, cratering efficiency increases with increasing size of the crater. This trend has been explained by a decrease in the effective target strength as the crater becomes larger (17, 18). In hardness tests of glass, the strength is known to increase as the dimensions of the tested area decrease (19).

Because the phenomena of impact on glass is similar to that on rock, our expression for displaced mass is compared with one derived by Gault (20) for dense crystalline rock. He finds $M_e = 1300\ E^{1.12}$ in the units used above. The mass of rock ejected is about six times that of glass for a given energy of impact. Rock is less homogeneous than glass; and, therefore, rock has a lower effective strength.

CONCLUSIONS

In conclusion, we find that the crater morphology changes markedly in the velocity range from 2 to 14 km/s for polystyrene microspheres impacting soda-lime glass targets. At 3 km/s, the rebounding projectile forms a shallow depression in the glass. The deformed projectile lines and overflows the depression from an impact at 4 km/s. At about 5 km/s, a petalled lip forms; and at a slightly higher velocity, a spallation region is generated outside the central cup. This region is characterized by radial and concentric fractures and radial ridges where the spalls have been ejected. As the velocity of impact increases further, the spallation zone becomes more finely fragmented. These transitions in morphology occur at higher velocities than for similar changes observed for impacts by denser projectiles. This indicates that the specific energy of the particle is a primary factor in the mechanics of crater formation. For constant velocity, the D_c/d ratio is independent of mass; but with velocity increasing from 5.2 to 14 km/s, the ratio increases from 1.25 to 1.75. The total mass of glass displaced per unit of the projectile energy increases slowly with energy in agreement with results of studies by others of craters formed by centimeter-size projectiles impacting rock.

In any application of these laboratory impact data to analysis of lunar microcraters, several points should be kept in mind. Although crater morphology can provide some information on the velocity and angle of incidence of the impacting particle, the threshold velocities for certain features of the crater depend on the projecile density and occur at lower velocities for higher density particles, In addition, for a

given projectile mass and crater shape, the low density particle produces a larger area of damage. Finally, ejected spalls may diminish the central cup in size, and a measurement of the diameter of the residual cup can lead to a low estimated value for the size of the impacting projectile. The probability of ejection of these spalls increases with increasing projectile size for a given velocity of impact.

ACKNOWLEDGMENTS

We thank D. E. Gault for his support and encouragement in the experimentation and his comments on this paper. W. L. Quaide and N. H. Farlow kindly reviewed the manuscript. Credit is due to K. Bozeman, M. I. Gottlieb, and R. Garrard for operation and maintenance of the accelerator, and to H. Lem for operating the SEM. Trapelo/West, a division of LFE Corporation, treated the targets in their low temperature asher. Numerous others helped to make this work a success.

REFERENCES

1. L. Secretan and O. E. Berg, A new criterion for the identification of micrometeor impact sites on aluminized glass, J. Geophys. Res. 74 (1969) 3681.
2. H. A. Zook, R. E. Flaherty, and D. J. Kessler, Meteoroid impacts on the Gemini windows, Planet. Space Sci. 18 (1970) 953.
3. D. S. Hallgren and C. L. Hemenway, Direct observation of particulate and impact contamination of "optical" surfaces in space, in: Space Research IX, edited by K. S. W. Champion, P. A. Smith, and R. L. Smith-Rose (North-Holland Publishing Co., Amsterdam, 1969) 102.
4. R. E. Garnon, T. S. Laszlo, and C. H. Leigh, Effects of micro-particle impact on the optical properties of metals, AIAA J. 3 (1965) 2096.
5. D. E. Gault, E. M. Shoemaker, and H. J. Moore, Spray ejected from the lunar surface by meteoroid impact, NASA TN D-1767 (1963).
6. D. E. Gault and J. A. Wedekind, The destruction of tektites by micrometeoroid impact, J. Geophys. Res. 74 (1969) 6780.
7. F. L. Whipple, The meteoritic environment of the moon, Proc. Roy. Soc. A (London) 296 (1967) 304.
8. F. Hörz, J. B. Hartung and D. E. Gault, Micrometeorite craters on lunar rock surfaces, in: The Geophysics of The Moon, ed. G. Simmons, to be published.
9. G. Neukum, A Mehl, H. Fechtig, and J. Zähringer, Impact phenomena of micrometeorites on lunar surface materials, Earth Planet. Sci. Letters 8 (1970) 31.

10. S. Auer, E. Grün, P. Rauser, V. Rudolph, and K. Sitte, Studies on simulated micrometeoroid impact, in: Space Research VIII, edited by A. P. Mitra, L. G. Jacchia, and W. S. Newman, (North-Holland Publishing Co., Amsterdam, 1968) 607.

11. J. F. Friichtenicht, Micrometeoroid simulation using nuclear accelerator techniques, Nucl. Instrum. and Meth. 28 (1964) 28.

12. V. Rudolph, Untersuchungen an Kratern von Mikroprojektilen im Geschwindigkeitsbereich von 0.5 bis 10 km/sec, Z. Naturforsch 24a (1969) 326.

13. M. Bloch, H. Fechtig, J. Funkhouser, W. Gentner, E. Jessberger, T. Kirsten, O. Müller, G. Neukum. E. Schneider, F. Steinbrunn, and J. Zähringer, Meteorite impact craters, crater simulations, and the meteoric flux in the early solar system, in: Proceedings of the Second Annual Lunar Science Conference, Geochim. Cosmochim. Acta, to be published.

14. J. F. Vedder, Microcraters in glass and minerals, Earth Planet. Sci. Letters (1971), to be published.

15. J. F. Vedder, Charging and acceleration of microparticles, Rev. Sci. Instr. 34 (1963) 1175.

16. H. Shelton, C. O. Hendricks, Jr., and R. F. Wuerker, J. Appl. Phys. 31 (1960) 1243.

17. H. J. Moore, D. E. Gault, and E. O. Heitowit, Change in effective target strength with increasing size of hypervelocity impact craters, in: Proc. 7th Hypervelocity Impact Symposium, IV (1965) 35.

18. D. E. Gault and H. J. Moore, Scaling relations for microscale to megascale impact craters, in: Proc. 7th Hypervelocity Impact Symposium, VI (1965) 341.

19. P. Walton, Micro- and macrostrength of glass: a review, in Mechanical Properties of Non-metallic Brittle Materials, ed. W. H. Walton (Interscience Publ., N. Y., 1958) 64.

20. D. E. Gault, Private communication (1971).

Table 1. Summary of data for polystyrene spheres impacting glass at normal incidence.

Projectile				Crater						
				Diameter		Depth			Displaced Mass	
Velocity (v, km/s)	Mass (m, pg)	Diameter (d, μm)	Energy (E, μJ)	Cup (D_C, μm)	Spall (D_S, μm)	Cup (P, μm)	D_C/d	D_S/d	Cup (M_{eC}, pg)	Total (M_{eS}, pg)
2.06	46.2	4.37	0.098	No crater found						
2.95	42.2	4.24	0.183	3.2	--		.76	--		
4.15	28.6	3.72	0.246	3.7	--	0.7	1.00	--		
4.9	31.8	3.86	0.382	4.5	--	0.4	1.16	--		
5.05	57.7	4.70	0.736	5.0	--	1	1.08	--		
5.1	62.1	4.82	0.807	5.0	--	1	1.04	--		
5.27	41.2	4.20	0.572	5.45	14	0.7	1.30	3.3	21	132.0
5.38	27.5	3.67	0.398	4.8	11	0.8	1.31	3.0	18.7	94.6
5.54	45.9	4.36	0.709	5.5	13	1	1.28	3.0	30.7	165.0
5.80	31.3	3.84	0.525	5.1	13	--	1.33	3.4	--	--
5.96	11.2	2.73	0.199	3.6	8	0.7	1.32	2.9	9.25	43.9
5.97	41.4	4.21	0.737	5.5	15	--	1.31	3.5	--	--
6.09	2.49	1.65	0.046	2.2	4.3	0.3	1.33	2.6	1.5	5.5
6.10	11.7	2.76	0.217	3.6	8	0.7	1.30	2.9	6.45	31.2
6.3	22.7	3.44	0.451	4.9	10	0.5	1.42	2.9	12.3	48.7
6.9	30.5	3.80	0.625	5.4	13	--	1.43	3.4	--	--
7.0	21.7	3.39	0.531	5.0	11.5	0.8	1.48	3.4	20	103.4
7.2	20.8	3.34	0.540	5.0	10	0.9	1.50	3.0	22.8	88.3
7.3	17.5	3.16	0.465	4.75	11	--	1.50	3.5	--	--
8.22	17.0	3.13	0.574	4.8	11.5	--	1.53	3.4	--	--
8.4	6.15	2.23	0.217	3.2	7.5	1.2	1.43	3.0	14.2	67.8
8.73	5.73	2.18	0.219	3.3	7	0.8	1.51	3.2	9.17	38.7
8.75	4.65	2.03	0.178	2.9	6	1.1	1.43	3.2	10.7	40.2
10.1	3.23	1.80	0.165	2.9	6.25	0.9	1.60	3.75	8.29	41.3
12.3	1.23	1.30	0.093	2.25	5	0.65	1.74	3.85	3.49	16.1
12.6	1.67	1.44	0.132	.4	4.75	1	1.66	3.4	6.88	23.7
14.0	0.70	1.08	0.069	1.9	3.5	0.7	1.75	3.3	2.89	8.8

Table 2. Summary of data for polystyrene spheres impacting glass at oblique incidence

Projectile				Crater			
Velocity (v, km/s)	Mass (m, pg)	Diameter (d, μm)	Energy (E, μJ)	Length (L, μm)	Width (W, μm)	Depth (P, μm)	Spallation
			θ = 45°				
4.85	56.6	4.67	0.665	7.5	5.5	0.4	No
5.54	19.8	3.29	0.304	5.2	4.5	0.3	No
5.71	53.8	4.59	0.877	8.7	7.0	1.0	No
5.91	26.3	3.62	0.469	6.8	5.5	0.4	No
6.3	44.4	4.31	0. 79	--	--	--	--
6.55	27.5	3.67	0.590	7.4	5.0	0.8	Yes
6.79	25.7	3.59	0.592	7.0	4.0	0.5	Yes
7.22	14.8	2.99	0.385	6.4	4.0	0.5	Yes
8.05	19.2	3.26	0.62	5.8	5.0	1.0	Yes
8.30	19.8	3.29	0.682	6.7	5.0	0.8	Yes
12.5	1.22	1.3	0.095	3.8	2.5	0.4	Yes
			θ = 30°				
5.1	59.0	4.74	0.768	--	--	--	--
6.0	31.7	3.8	0.570	6.0	4.0	0.25	No
6.4	40.3	4.17	0.825	7.0	5.5	0.25	No
6.9	7.91	1.99	0.188	--	--	--	--
7.2	17.9	3.18	0.464	6.5	4.0	0.6	Yes
7.8	17.0	3.13	0.517	7.3	4.5	0.5	Yes
8.4	12.3	2.81	0.434	5.5	4.0	0.5	No
12.3	1.22	1.3	0.092	3.1	2.3	0.25	No

Table 3. Comparison of the impact velocities for occurrence of several morphological features of craters formed in soda-lime glass by projectiles with differing densities.

Projectile Density (g/cm^3)	Projectile Material	Morphology			
		Dented Glass (km/s)	Deformed Projectile (km/s)	Petalled Lip (km/s)	Spallation (km/s)
1.06	Polystyrene[a]	3	3.5-4.6	4.8-7	> 5.2
2.7	Aluminum[b]	?	?	?(<3.6)-7	> ? (<3.6)
7.8	Iron[c]	< 1	1-2	> 3	> 3

a. Information is included from some additional impacts not listed in table 1.
b. Taken from ref. 14.
c. Taken from ref. 9.

FIGURE CAPTIONS

Fig. 1 SEM photomicrographs of craters formed by polystyrene spheres striking soda-lime glass at normal incidence ($\theta = 90°$)

a) 2.95 km/s, 42.2 pg, SEM stage tilt T = 30°;

b) 4.15 km/s, 28.6 pg, T = 30°;

c) 5.05 km/s, 57.7 pg, T = 23°;

d) 5.38 km/s, 27.5 pg, T = 30°;

e) 8.22 km/s, 17.0 pg, T - 23°;

f) 12.6 km/s, 1.67 pg, T = 23°.

The SEM stage tilt is such that the top of each micrograph is at the base of the slope.

Fig. 2 SEM micrographs of craters formed by polystyrene spheres striking soda-lime glass at oblique incidence.

a) 7.2 km/s, 15 pg, $\theta = 45°$, T = 30°;

b) 7.8 km/s, 17 pg, $\theta = 30°$, T = 30°.

Fig. 3 The ratios of the diameter of the spallation zone to the projectile diameter (D_S/d) and the central cup diameter to the projectile diameter (D_C/d) versus projectile velocity for polystyrene spheres impacting glass at normal incidence ($\theta = 90°$).

Fig. 4 The ratios of the diameter of the spallation zone to the projectile diameter (D_S/d) and central cup diameter to projectile diameter (D_C/d) versus projectile mass for different velocity intervals of polystyrene spheres impacting glass at normal incidence.

Fig. 5 The diameters of the crater cup (D_C) and the spallation zone (D_S) versus projectile mass for polystyrene spheres striking glass at normal incidence.

Fig. 6 Displaced mass of target material versus projectile kinetic energy in microjoules calculated for the central cup (M_{eC}) and for the whole area of damage (M_{eS}) for polystyrene spheres striking glass at normal incidence.

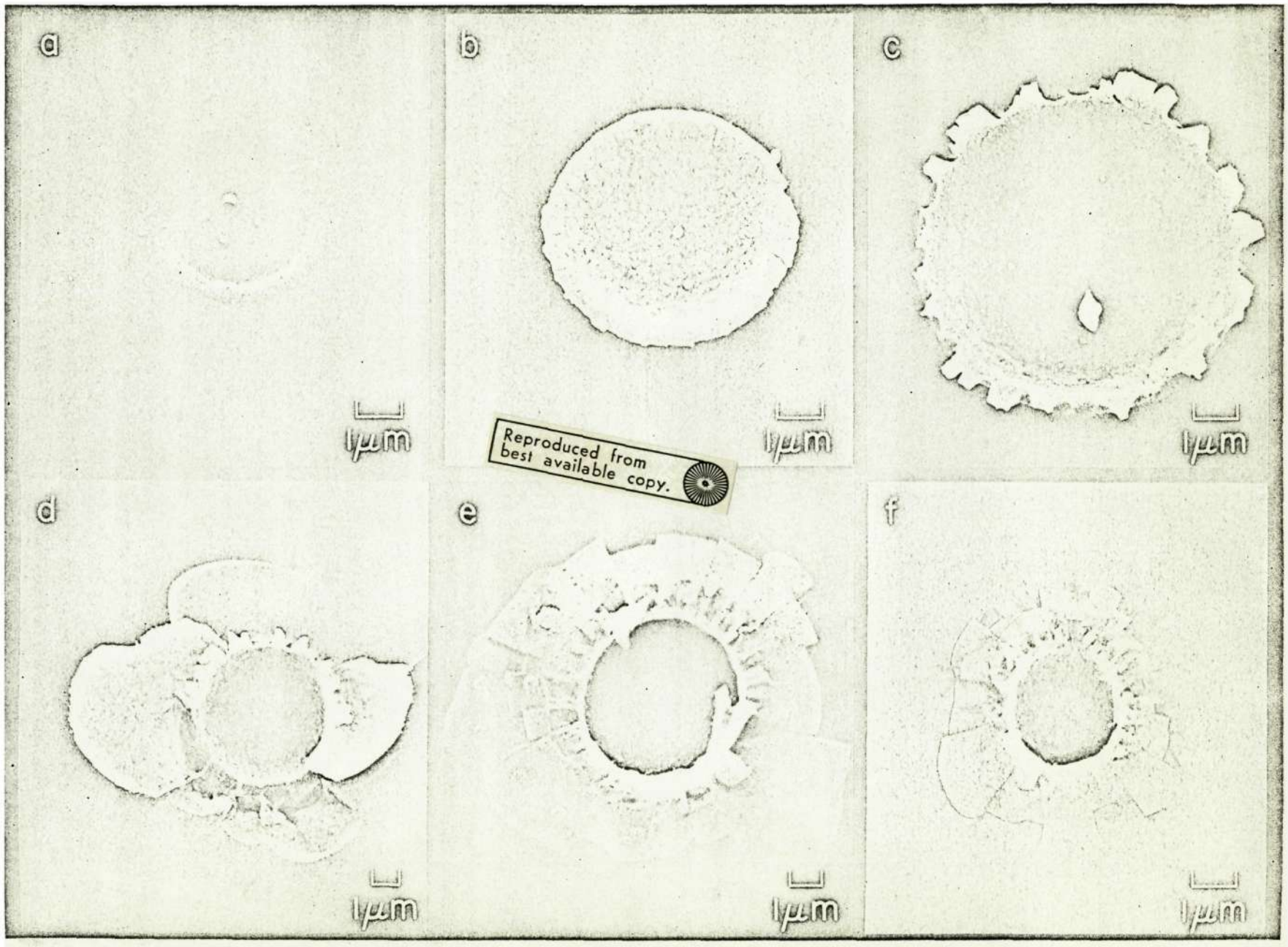

NATIONAL AERONAUTICS AND SPACE ADMINISTRATION
AMES RESEARCH CENTER, MOFFETT FIELD, CALIFORNIA

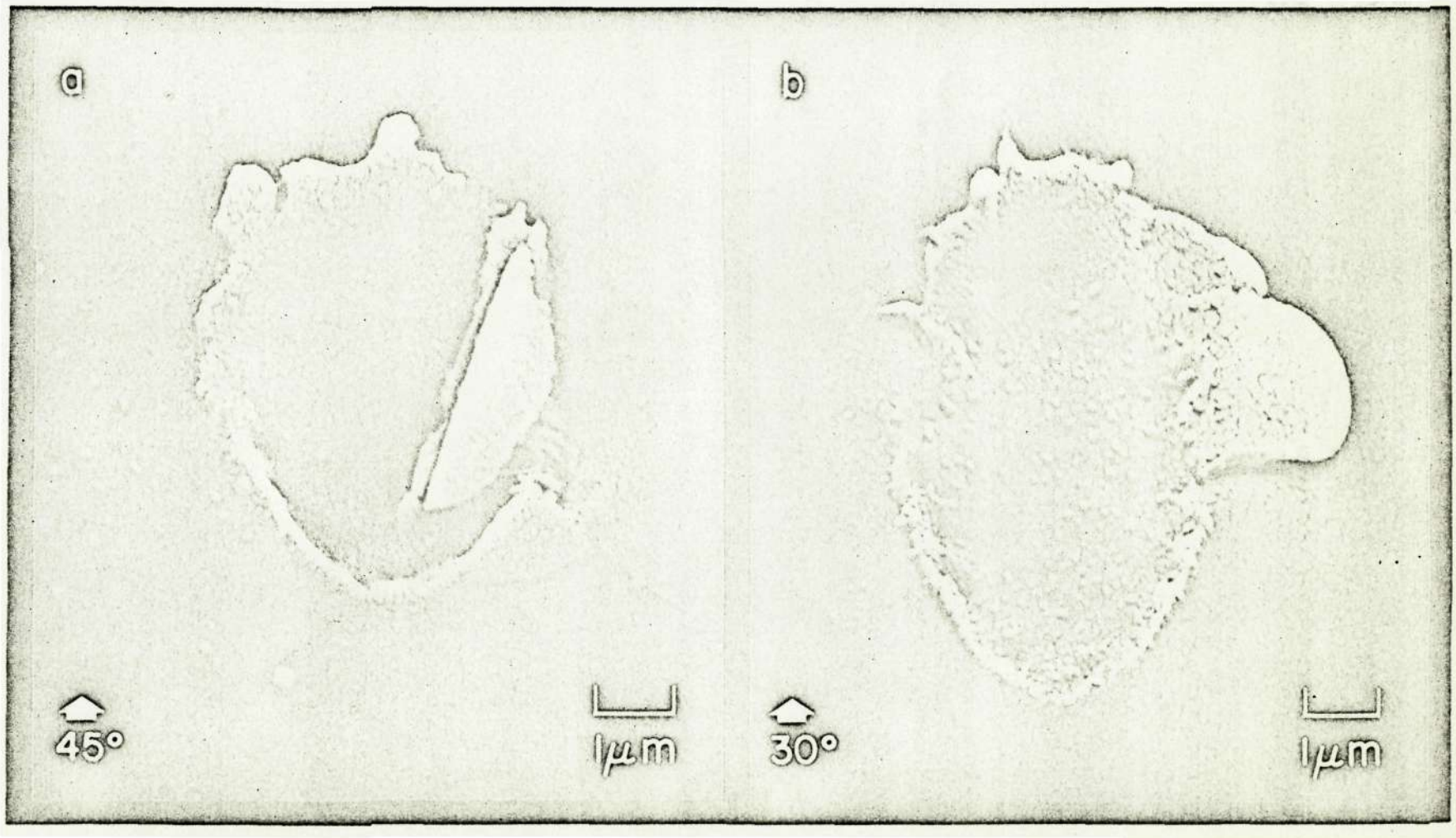

NATIONAL AERONAUTICS AND SPACE ADMINISTRATION
AMES RESEARCH CENTER, MOFFETT FIELD, CALIFORNIA

P.S. ⟶ GLASS

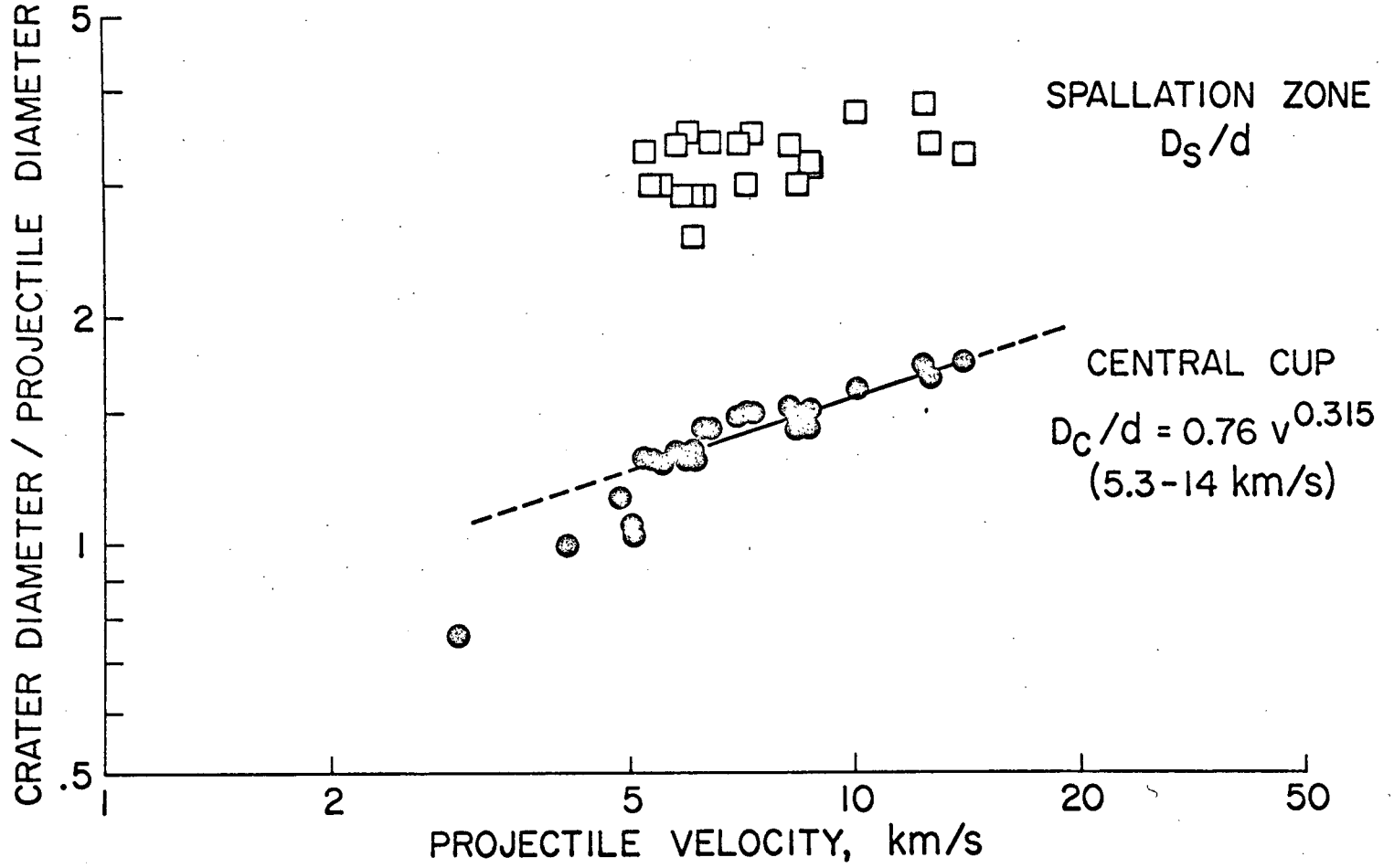

NATIONAL AERONAUTICS AND SPACE ADMINISTRATION
AMES RESEARCH CENTER, MOFFETT FIELD, CALIFORNIA

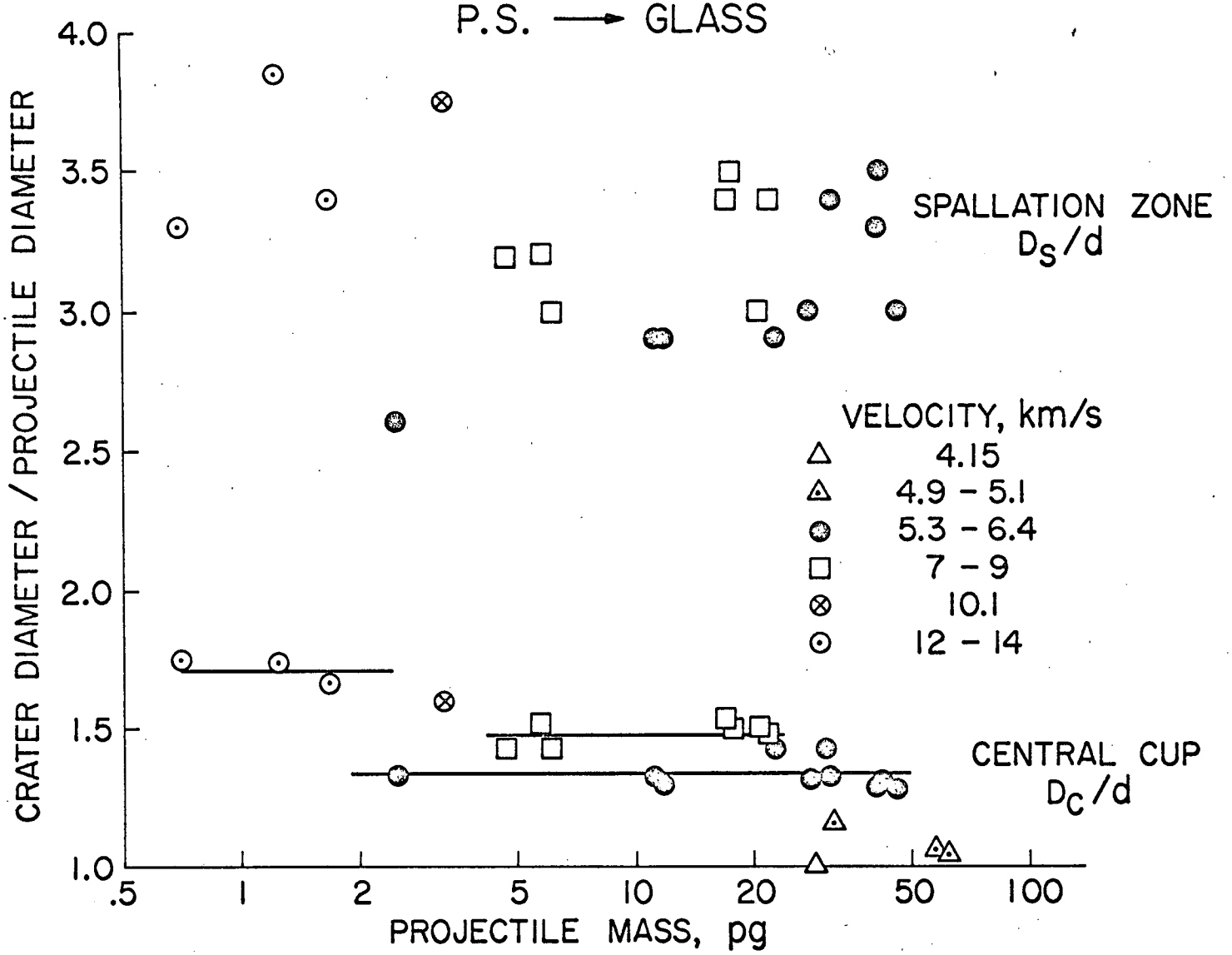

NATIONAL AERONAUTICS AND SPACE ADMINISTRATION
AMES RESEARCH CENTER, MOFFETT FIELD, CALIFORNIA

P.S. ⟶ GLASS

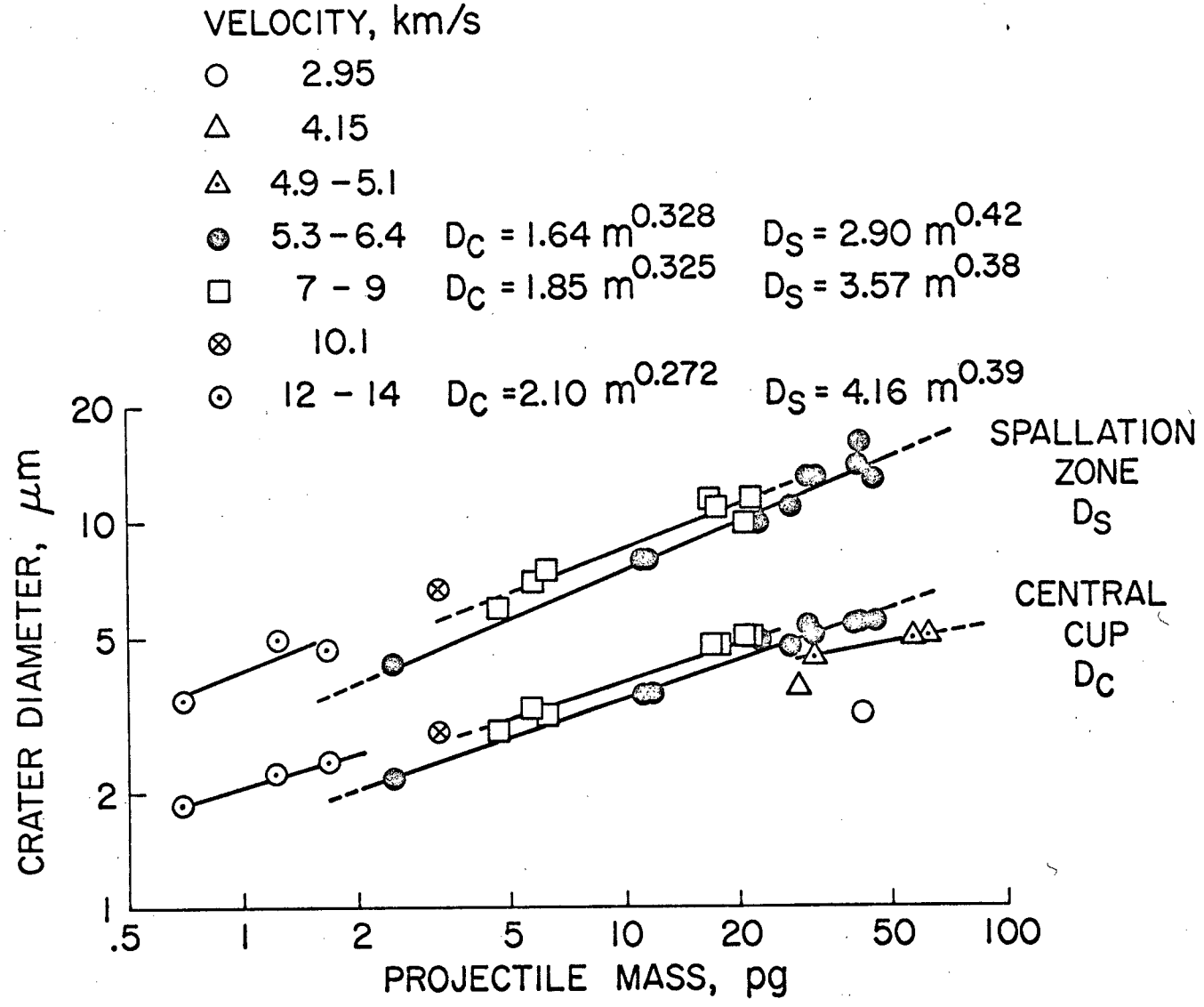

NATIONAL AERONAUTICS AND SPACE ADMINISTRATION
AMES RESEARCH CENTER, MOFFETT FIELD, CALIFORNIA

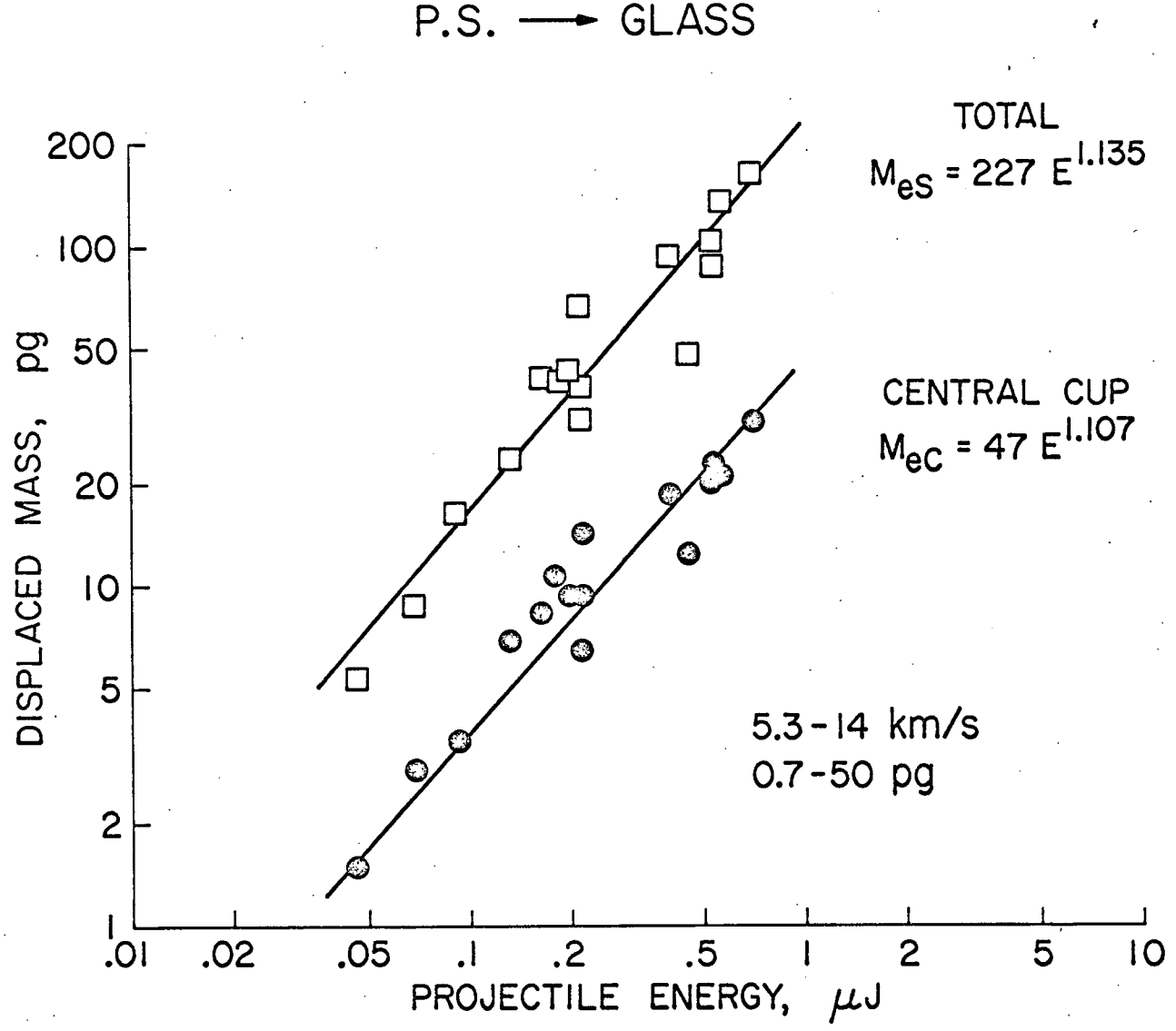

NATIONAL AERONAUTICS AND SPACE ADMINISTRATION
AMES RESEARCH CENTER, MOFFETT FIELD, CALIFORNIA